SSC21-XI-05

Cu-Enhanced 3-D Printed Fuels for Green SmallSat Propulsion

Stephen A. Whitmore & Kurt C. Olsen
Utah State University, Mechanical and Aerospace Engineering Department
4130 Old Main Hill, Logan UT 84322-4130; +01-435-760-0221
Stephen.Whitmore@usu.edu

Victoria L. Coverstone & Cagri Y. Oztan
University of Miami, Mechanical and Aerospace Engineering Department
1251 Memorial Drive, McArthur Engineering Building
Coral Gables FL 33146, +01-305 284-3316
vcoverstone@miami.edu

ABSTRACT

The Propulsion Research Laboratory at Utah State University (USU) has recently developed a promising High-Performance "Green" Hybrid Propulsion (HPGHP) technology that derives from the novel electrical breakdown property of certain 3-D printed like acrylonitrile butadiene styrene (ABS). This electrical breakdown property has been engineered into a proprietary, power-efficient system that can be cold-started and restarted with a high degree of reliability. One of the issues associated with ABS as a propellant is its low burn rate. It is well documented in technical literature that hybrid rocket systems generally have fuel regression rates that are typically 25-30% lower than solid fuel motors in the same thrust and impulse class. Lowered fuel regression rates tend to produce unacceptably low equivalence ratios that lead to poor mass-impulse performance, erosive fuel burning, nozzle erosion, reduced motor duty cycles, and the potential for combustion instability. To achieve equivalence ratios that produce acceptable combustion characteristics, hybrid fuel ports are often fabricated with large length-to-diameter ratios. The resulting poor volumetric efficiency is incompatible with Small Satellite (SmallSat) applications.

This paper presents preliminary results from a collaborative development program between the University of Miami (UM) and USU. In this reported work, modern extrusion and 3-D printing techniques are used to fabricate sample ABS fuel grains with varying levels of copper-metallization. Hybrid-ABS fuel grains were printed from Cu-infused feed stock with 2%, 4%, and 6% Cu-mass concentrations. As baseline control, 100% pure ABS fuel grains (0% Cu) were also printed. Heat conduction via the additive copper (Cu) provides an efficient heat transfer mechanism that augments surface convection from the flame zone. Forced convection, the primary mechanism for pyrolysis for hybrid fuels, is generally inefficient due to "wall-blowing" associated with the radially emanating massflow from fuel pyrolysis. Wall-blowing pushes the flame zone away from the fuel surface and significantly reduces the rate of enthalpy exchange. Homogeneously mixing a high conductivity metal such as Cu into the ABS fuel provides an efficient heat transfer mechanism, and allows radiant heat from the flame zone to be transferred deep into the fuel material. This process significantly increases the pyrolytic efficiency of the fuels.

The Cu-infused fuels were tested at USU using a legacy 12-N hybrid thruster system. Fabrication and manufacturing methods are described, and results of hot fire tests are presented. The top-level conclusion is that Cu-infusion of the printed fuels measurably increases the fuel regression rate, allowing for a higher thrust level with no increase in the required volume. The Cu-infusion has negligible impact on the propellant characteristic velocity and the overall system specific impulse. The increased burn rate and overall increase in solid-fuel density resulting from Cu-infusion allows a measurable increase in the propellant impulse-density. This increase in volumetric efficiency is potentially significant for small spacecraft applications where available space has a premium value. Follow-on methods that infuse lower-molecular weight and higher thermal conductivity materials like graphene and carbon-nanotubes are proposed.

INTRODUCTION AND BACKGROUND

This paper presents preliminary results from a collaborative development program between the University of Miami (UM) and Utah State University (USU). In this development campaign, modern extrusion and 3-D printing techniques are used to fabricate sample ABS fuel grains with varying levels of copper-metallization. The fabricated fuels are currently being

tested by USU's Propulsion Research laboratory using a legacy 38-mm, 12-N hybrid thruster system previously designed for small spacecraft applications.[1,2,3] Fabrication and manufacturing methods are described, and results of hot fire tests are presented. The top-level conclusion is that metallization of the printed fuel grains moderately increases the fuel regression rate, with negligible impact on the propellant characteristic velocity and the overall system specific impulse. The increased burn rate and overall increase in solid-fuel density resulting from metallization will allow a measurable increase in the propellant impulse-density. This result is potentially significant for small spacecraft and other applications where volumetric efficiency has a premium value.

It is well documented in technical literature that hybrid rocket systems generally have fuel regression rates that are typically 25-30% lower than solid fuel motors in the same thrust and impulse class.[4] Lowered fuel regression rates tend to produce unacceptably low equivalence ratios that lead to poor mass-impulse performance, erosive fuel burning, nozzle erosion, reduced motor duty cycles, and potential combustion instability. To achieve equivalence ratios resulting in acceptable combustion characteristics, hybrid fuel ports are often fabricated with very long length-to-diameter ratios. The resulting poor volumetric efficiency is incompatible with Small Satellite (SmallSat) applications.

Existing Regression-Rate Enhancement Methods

To date the most attempts to increase the fuel regression rates have relied upon mechanical enhancement methods including complex internal port geometries with multiple fuel ports.[5] There are several issues associated with this multi-port approach. First, there is a significant potential for uneven port burning that presents a significant potential for compromised fuel grain integrity, especially towards the end of the burn. There is often a requirement for an embedded structure to support the fuel port as it regresses. The presence of this supporting web adds complexity to the fuel port design, and has the potential to allow voids within the fuel grain structure. Such voids can contribute to the potential for fuel grain fractures.[6] Second, multi-port fuel grain designs typically produce unburned mass fractions greater than 10%. Third, multiple port designs present an increased risk of feed-coupling instabilities related to dynamic flow interactions between the injector(s), the multiple fuel ports, and the pre-combustion chamber.[7]

Whitmore et. al (2014)[8] and Whitmore and Walker[9] have investigated the use of 3-D printing to embed helical structures into the fuel port. Centrifugal forces generated by the helix force the flame zone against the fuel all; thereby suppressing "wall-blowing" due to the radial outflow from the fuel pyrolysis, and increases the fuel regression rate. This approach has demonstrated up to a 5-fold increase in the initial fuel regression rate; however, because the port rabidly burns to a circular cross section, the regression rate increase is only temporary. The associated drop in regression rate promotes a significant oxidizer-to-fuel ratio shift, and helical port motors generally burn at very low equivalence ratios near the endo of the burn lifetime. This large O/F shift may be difficult to manage for small thruster configurations.

Swirl injection has been demonstrated to be effective in increasing the fuel regression rate.[10,11] Swirl injectors are able to reduce both thickness and growth of the boundary layer, thus enhancing heat transfer. The heat transfer variation is reduced and regression rate is more uniform. Some effects of swirling must be addressed, including induced torque and effects of non-axial flow in the nozzle (effective throat area and divergence losses). No swirl or vortex injection hybrid motor has ever been flight-tested. The effects of motor acceleration upon the swirl effectiveness has yet to be assessed.

Finally, Karabeyoglu, et al.,[12] have investigated a class of hybrid fuel materials based on paraffin wax formulations. These paraffin-based fuels melt before vaporizing, and a properly formulated wax mix produces a melt layer with a low viscosity and high surface tension. When the oxidizer flows at high speed over the upper side of the melting fuel surface, the liquid layer becomes unstable and minute surface waves are formed. The resulting fluid boundary layer is hydro-dynamically unstable and allows fuel droplets to be entrained into the core flow. The entrained fluid droplets significantly increase the massflow generated by the ablating fuel, but does not increase the "blowing-effect" that suppresses regression rate due to the ablating radial massflow.

For stable oxidizer flux levels droplet entrainment massflow is significantly greater than massflow resulting from direct gasification. Paraffin-based fuels have been developed that burn at surface regression rates three to four times that of conventional hybrid fuels.[13] The high regression rate hybrid removes the need for a complex multiport grain, and most applications up to large boosters can be designed with a single port configuration. Karabeyoglu, et al. have ground-tested paraffin fuel hybrid rocket motors large as 60 cm in diameter.[14] The primary issue associated with liquefying fuels is the reduced combustion efficiency as unburned

propellants are shed by the rocket plume. This drop in combustion efficiency significantly reduces the flame temperature and the effective raises exhaust molecular weight. Generally, liquefying propellants produce significantly lower specific impulse values when compared to more conventional gasifying propellants.

Metallization as a Potential Hybrid Fuel Regression Enhancement Technique

It is well known that adding fine-grain aluminum particles to conventional AP-composite solid rockets propellants significantly increases the burn flame temperature. This flame temperature increase offsets the associated increase in molecular weight due to the added metal. The result is a significant increase in performance including propellant density, characteristic velocity, and specific impulse.[15]

However; this result does not necessarily translate to hybrid rocket fuels. Karabeyoglu and Arkun[16] present a detailed summary of potential additives. These authors generally conclude that conventional aluminum and aluminum-oxide powders, as are conventionally added to solid propellant fuels, are generally ineffective for increasing hybrid fuel regression rates. The lack of oxidizer and combustion beneath the flame zone limits the effectiveness of metal combustion. Also, introducing metal particles generally increases the exhaust product molecular weights and results a marginal drop in the end-to-end motor performance, especially when higher performance oxidizers are used. A primary concern of Ref. [16] and is the ability to achieve uniform fuel grain properties during the metallization process.

The proposed method will not attempt to enhance the thermodynamics of the combustion process; but instead by homogeneously mixing a high conductivity metal such as copper (Cu) into the fuel, an additional efficient transfer mechanism is added to the regression process. Typically, for a thermoplastic or rubberized material, heat transfer to the fuel grain surface results primarily from forced convection from the core combustion flame. As described earlier, the convection process is generally inefficient due to the radially emanating massflow from fuel pyrolysis. This "wall blowing" pushes the flame zone away from the fuel surface and results in a significantly reduced rate of enthalpy exchange. The "air hockey" effect from the pyrolytic layer also suppresses the surface skin friction, limiting the Reynold's stresses and the associated rate of convective heat transfer. The addition of conduction as a heat transfer mechanism has significant potential to enhance the overall fuel regression rate. Here the fuel surface captures radiant heat from the flame zone and transfers it deep into the fuel material. This process significantly increases the pyrolytic efficiency of thermo-plastic fuels.

Fuel Grain Metallization Methodology

Figure 1 shows the multistep strategy that was employed to followed to fabricate the copper enhanced Acrylonitrile Butadiene Styrene (ABS) fuel grains. As a starter commercial CYCOLAC MG94 Resin[17] ABS pellets, were procured from Filastruder, USA.[18] The pellets were cryogenically ground into fine powder to ensure uniform mixing with the 350 mesh copper powder procured from EnvironMolds, LLC.[19] For these tests the ABS and Cu were mixed in three different concentrations by weight: 2, 4, 6 percent. The mixed powers were extruded into custom filaments with an average diameter of 1.75 mm using a commercial

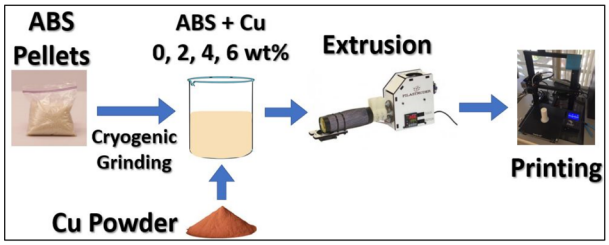

Figure 1. Process for Fabricating Cu-Infused ABS Fuel Grains.

extruder (Filastruder Inc), at an extrusion temperature of 220 ^{o}C.

To achieve high diametric precision, each type of filament was wound on a separate spool using Filawinder (Filastruder Inc) spooling system. The resulting Extruded filaments were used as stock materials for a Creality Ender 3[20] Fused Deposition Manufacturing (FDM) printer. The fuel grains were printed in a line pattern at 100% infill density using an 0.8 mm nozzle. Layer height, printing speed and printing temperature were set to 0.4 mm, 50 mm/s and 250 ^{o}C, respectively. The temperature of the deposition build plate was maintained at 100 ^{o}C. Double sided tape was applied on the build plate to ensure better adhesion.

TEST HARDWARE AND TEST PROCEDURES

This section descries the metalized grain geometries that were printed. Detailed port images will be presented. The interface to the legacy 38-mm thruster system is described, and a brief overview of the test apparatus and instrumentation system sis presented. Of particular

emphasis is the modification required to use the metallized grains with USU's patented hybrid arc-ignition system. Interface to the arc ignition system required that a separate ignition cap be printed and attached to the top of the metalized fuel grans. The injector cap geometry and function will be described in detail.

3-D Printed Fuel Port Designs

As described in the previous section, fuel grains were printed from the extruded feed stock with 2%, 4%, and 6% Cu-mass concentrations. As baseline control, 100% pure ABS fuel grains (0% Cu) were also printed. Multiple samples of each configuration were printed and tested for each of the copper concentrations. The Cu-infused fuels were all printed at 100% in-fill density. Random density measurements on the resulting 3-D prints indicated very-low variation in material density. The associated densities of the control (0%), 2%, 4%, and 6% fuel grains were *1.039 g/cm*^{3}, *1.058 g/cm*^{3}, *1.077 g/cm*^{3}, *1.097 g/cm*^{3}, respectively.

Fuel grains with two different fuel port geometries (1) a cylindrical fuel port and (2) a 6-lobed star fuel port cross-section, were manufactured and tested. Table 1 summarizes these port geometries. Figure 2 compares the 6-lobed star cross-section against the cylindrical fuel port, with all displayed dimensions in units of millimeters. The total cross-sectional area of the 6-lobed star port is *22 mm*^{2}. The effective hydraulic diameter of the star port configuration based on flow area is approximately 5.3 *mm*. The cross-section area of the cylindrical port was significantly larger, *50.27 mm*^{2} with an *8-mm* diameter cylindrical port. Each of the fuel grains had a standard external diameter of *34 mm and a length of 40 mm*.

Table 1. 3-D Printed Fuel Port Configurations.

Port Design	Properties	
Cylindrical Port	Initial Port Diameter	*8 mm*
	Initial Cross Sectional Are	*50.27 mm*^{2}
6-lobed Star Port	Inner Diameter	*2.67 mm*
	Effective Hydraulic Diameter based on Area	*5.2 mm*
	Initial Cross Sectional Area	*22.0 mm*^{2}

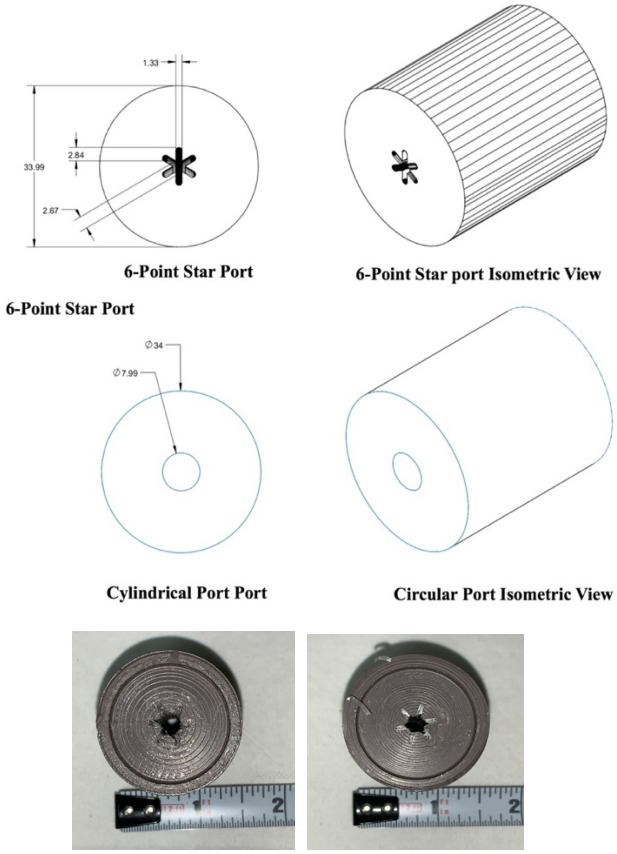

Figure 2. 3-D Printed Port Geometries.

Description of the Test Article

This section presents descriptions of the legacy thruster system used for this testing campaign. The presented discussion is a top-level summary. Whitmore and Stoddard,[21] Stoddard,[22] and Whitmore[23] discuss the legacy hardware development and the associated testing campaigns in significantly greater detail.

Thrust Chamber

The legacy 38-mm diameter *GOX/ABS* thruster prototype from Ref. [21] was reconfigured this testing campaign. The thruster system as tested, closely matched the flight-weight systems described by Ref. [3] For this study a highly-purified grade of *gaseous oxygen (GOX*) was used to ensure that the resulting flow path was free from contaminants and any other possible catalytic agents. The images of Figure 3 present the details of the thrust chamber assembly showing the top and side view schematics and the major system assembly components; *1*) graphite nozzle, *2*) nozzle retention cap, *3*) motor case, *4*) 3D printed fuel grain with embedded electrodes, *5*) insulating phenolic liner, *6*) chamber pressure fitting,

and 7) single-port injector cap. The 38-mm diameter motor case, constructed from 6061-T6 aluminum, was procured commercially. For this test series the injector and oxidizer feed pressures were set to produce approximately 10 N of thrust using the cylindrical fuel port. The 6-lobed star fuel ports using the same oxidizer feed pressure produced a slightly higher thrust level, approximately 12-N.

a) Top and Side-View Schematics

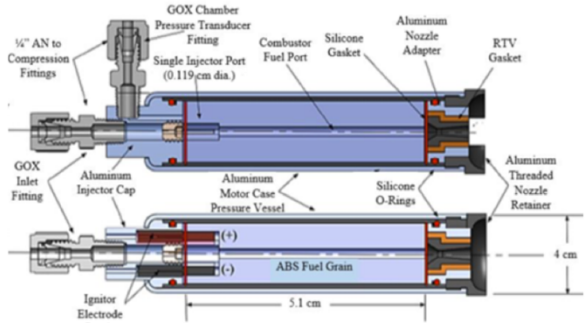

b) Assembly Components Assembly

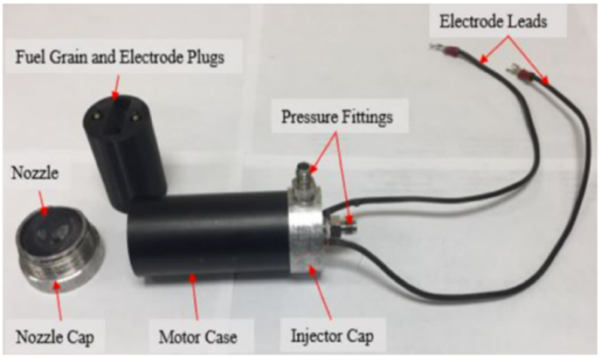

Figure 3. Legacy 38-mm, 12-N Test Article.

Arc Ignition System

The USU propulsion research laboratory has developed a unique low-wattage, non-pyrotechnic ignition system for hybrid rockets. This approach leverages the leveraging the unique electrical breakdown properties of 3-D printed thermoplastics like ABS. The authors discovered that when printed using a technique known as fused deposition modeling (FDM),[24] ABS possesses unique electrical breakdown properties that can be exploited to allow for rapid on-demand ignition.[25] Under normal conditions ABS possesses a very high electrical resistivity and is not generally considered as an electrical conductor.

However, as FDM-processed ABS is subjected to a moderate electrostatic potential between electrodes embedded in the material, the layered FDM structure concentrates electrical charges at points along the surface. The result is an inductive arc carving a path across the fuel surface.[26] Because Joule heating pyrolizes a small mass of fuel material, when an oxidizing flow is introduced at oxygen partial pressures above two atmospheres (Ref. [25]), combustion is initiated with the pyrolized vapor. As developed over the past five years, the HPGHP arc-ignition system is extremely power-efficient and can be started, stopped, and restarted with a high degree of reliability.[27] Once started, the system can be sequentially fired with no additional energy inputs required. Multiple prototype ground-test units with thrust levels varying from 4.5 N to 900 N have been developed and tested.[28,29]

Figure 4 shows the details of the arc-ignition system. Fig. 4(a) shows a typical fuel grain head end layout with flow impingement shelves and embedded electrodes in the 3-D printed ABS fuel grain. Fig. 4(b) shows the ignition system electronics schematic. The ignition system power processing unit is based on the UltraVolt® line of high-voltage power supplies (HVPS), Anon. Advanced Energy, (2019) [30]. The HVPS provides a current-limited (30 mA) high voltage output of up to 1000 V or 30 Watts total output power. Depending on the impedance on the arc-track between the ignitor electrodes, the dissipated voltage typically varies between 100 and 400 volts. Ignition power to the thruster is initiated by sending a TTL-level logic bit across a digital bus to activate to the HVPS.

a) Fuel Grain Head-End Ignitor Section Geometry

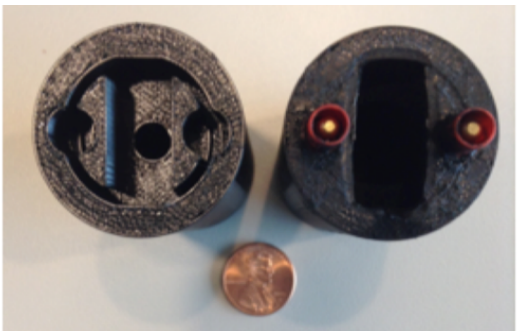

b) Schematic of Arc-Ignition System Electronics

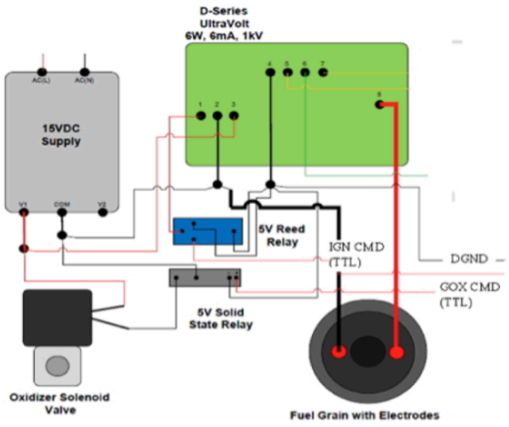

Figure 4. Details of the Legacy Thruster Arc-Ignition System.

The ignition system of Fig. 4 relies on the 3-D printed material impedance being within a proper range to allow current to pass through the material, while still offering sufficient electrical resistance to pyrolyze some material through the Joule-heating process. Mathias et. al[31] demonstrate that the ideal material impedance between the electrodes lies in a range between 50 kΩ and 500 kΩ. This impedance range also insulates the external metallic motor case from the HVPS-provided current.

However; when the ABS grains are copper-infused, the impedance of the material drops significantly, well-below the known optimal range. When this material is subjected to the HVPS-provided charge, the material acts as a closed circuit with current running though the material and straight to the surrounding motor case. Thus, the metal-augmented fuel grains cannot be directly sparked. Instead, a non-infused 100% abs ignition cap was printed and bonded to the top of the Cu-Infused fuel.

Figure 5 shows this configuration. The ignition cap head end emulates the "tried-and-true" arc-ignition geometry depicted by Fig. 4a. The depicted "slots" shown by Figure 5 are used to insulate the electrode wire paths in order to prevent current leakage to the grounded injector cap. A positive bonding surface is provided by a lip printed into the cap surface. This lip inserts into a cylindrical port machined into the top of the Cu-Infused fuel grain.

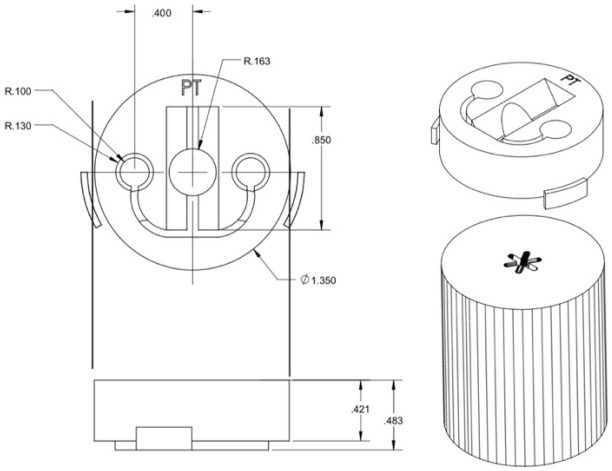

Figure 5. Arc-Ignition Cap Design and Interface to Cu-Infused ABS Fuel Grain.

For this application, the ignition cap was press-fit into the Cu-infused fuel grain and the package was held tight by the threaded nozzle retainer. This approach was used because it allowed the cap and fuel grains to be separated and weighed independently following each burn. Allowing independent mass measurements for these two components provides a more accurate calculation of the true Cu-infused fuel grain regression rates. For a flight application, the ignition cap would likely be bonded to the fuel grain using an industrial-grade ABS cement to secure the interface.

Test Stand and Instrumentation

Figure 6 shows the piping and instrumentation diagram (P&ID) of the test systems. The test stand measurements include Venturi-based oxidizer massflow measurements, load-cell based thrust measurements, chamber pressure, and multiple temperature readings at various points along the flow path. Directly aft of the thrust chamber lies the solenoid actuated oxidizer run-valve. Parameters measured include ignition power, thrust, chamber pressure, massflow, fuel regression rate, specific impulse, and impulse density.

Hot Fire Test Procedures

Pre-test measurements included fuel grain weight, and port diameter measured at both the top and bottom of the fuel port. The nozzle throat and exit plane

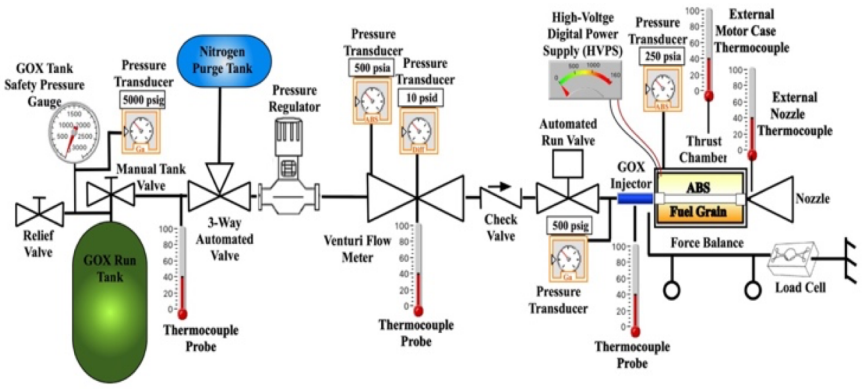

Figure 6. Test Stand Piping and Instrumentation Diagram.

diameters were also measured. Finally, the initial oxidizer run-tank tank weight, pressure, and temperature were measured. All data were logged on a spreadsheet for post-test analysis. The upstream oxidizer flow regulator feed pressure was manually set to approximately 2400 kPa (350 psig) in order to choke the injector and ensure a constant oxidizer massflow throughout the burn. In order to ensure ignition reliability of the Cu-infused grains, the HVPS was activated sending power to the fuel grain electrodes one second before the oxidizer run valve was opened. Once the run valve opened, then HVPS power to the electrodes was continued to overlap for another 1 second. Since the required power was so small, no attempt to shorten or optimize the "spark" length or overlap time was performed for this test series. For this test series, the motor run valve was programmed to open for a prescribed amount time that varied from 1 to 5 seconds. The motor would snuff immediately after closure of the run valve. Allowing for a safety margin to prevent motor-case burn through, one fuel grain allows for 9 seconds of total burn time. Thus, on a single fuel grain a typical test series would prescribe three tests of 3 seconds each. Following each burn, the weight and geometry measurements described in the previous paragraphs were repeated and logged for post-test analysis

DATA ANALYSIS METHODS

This section details the analytical methods that were used to calculate key derived-parameters from the raw test data. These mass-flow based calculations include 1) oxidizer massflow, 2) mean fuel regression rate, 3) oxidizer-to-fuel ratio, 4) mean fuel port diameter, 5) oxidizer massflux, 6) total massflux, 7) equivalence ratio, and 8) specific gravity. Key performance parameters calculated from the raw data include 1) combustion efficiency, 2) thrust coefficient, 3) specific impulse, 4) characteristic velocity, and 5) impulse density. The following section details how these calculations were performed. The presented calculations for regression rate, fuel port diameter, and massflux are valid only for the longitudinal averages. There is no attempt to spatially resolve these parameters along the length of the fuel port.

Calculating the Fuel Massflow Rate.

Although the inline Venturi measures the oxidizer massflow in real-time, the test stand was not configured to directly measure the fuel massflow. Instead, before and after each hot-firing the fuel grains were weighed to give the total fuel mass consumed during the test. As will be described later in this section, these mass measurements were used to anchor the "instantaneous" fuel massflow rates, calculated as the difference between the nozzle exit and oxidizer massflows,

$$\dot{m}_{fuel} = \dot{m}_{total} - \dot{m}_{ox} \quad (1)$$

Knowing the nozzle throat area A^* and the plume exhaust gas properties, the nozzle exit (total) massflow at each time point was calculated from the measured chamber pressure time history P_0, using the 1-dimensional choking massflow equation, (Anderson[32], Chapter 4)

$$\dot{m}_{total} = A^* \cdot P_0 \cdot \sqrt{\frac{\gamma}{R_g \cdot T_0} \cdot \left(\frac{2}{\gamma+1}\right)^{\frac{\gamma+1}{\gamma-1}}} \quad (2)$$

The calculation of Eq. (2) assumes the flow composition is frozen at the nozzle entrance and nozzle erosion during the burn.

A table of thermodynamic and transport equilibrium properties of the GOX/ABS and Nytrox/ABS exhaust plumes were calculated using NASA's CEA code[33] with chamber pressure P_0 and mean O/F ratio as independent look up variables for the tables. For each data point in the burn time history, the two-dimensional tables of thermodynamic and transport properties were interpolated using chamber pressure P_0 and mean O/F

ratio as lookup variables. Calculated parameters included the gas constant R_g, ratio of specific heats γ, and flame temperature T_0. Defining the combustion efficiency as

$$\eta^* = \frac{c^*_{actual}}{c^*_{ideal}} = \frac{\sqrt{\left(\frac{\gamma+1}{2\cdot\gamma}\right)^{\frac{\gamma+1}{(\gamma-1)}} R_g \cdot T_{0_{actual}}}}{\sqrt{\left(\frac{\gamma+1}{2\cdot\gamma}\right)^{\frac{\gamma+1}{(\gamma-1)}} R_g \cdot T_{0_{ideal}}}} \approx \sqrt{\frac{T_{0_{actual}}}{T_{0_{ideal}}}} \quad , \tag{3}$$

the theoretical flame temperature $T0_{ideal}$ was scaled by adjusting the combustion efficiency

$$T_{0_{actual}} = \eta^{*2} \cdot T_{0_{ideal}} \quad , \tag{4}$$

such that the calculated fuel mass consumption

$$\Delta M_{fuel} = \int_0^t \left(\dot{m}_{total} - \dot{m}_{ox} \right) dt \tag{5}$$

matched the measured value from differences of the pre- and post-test weight measurements. As described earlier, the consumed fuel mass anchored the thermodynamic calculations.

Adjusting input combustion efficiency upwards has the effect of increasing the calculated fuel mass consumption, and downwards decreases the calculated fuel mass consumption. The calculations of Equations (2-5) were iterated, adjusting η^* after each iteration, until the calculated fuel mass matched the measured mass within a prescribed level of accuracy, in this case 0.5%. For each iteration, the time-averaged *oxidizer-to-fuel* ratio was calculated as integrated oxidizer massflow divided by the consumed fuel mass,

$$\overline{O/F} = \frac{\int_0^{t_{burn}} \dot{m}_{ox}(t) \cdot dt}{\Delta M_{fuel}} = \frac{\int_0^{t_{burn}} \dot{m}_{ox}(t) \cdot dt}{\int_0^{t_{burn}} \left[\dot{m}_{total}(t) - \dot{m}_{ox}(t) \right] \cdot dt} \quad . \tag{6}$$

Calculating the Fuel Regression Rate

Once the massflow and consumed masses were calculated as described above, the mass-based mean longitudinal mean of the total fuel regression is derived from

$$\Delta M_{fuel} = \bar{\rho}_{fuel} \cdot L_{port} \left[\left(A_{port} \right)_{final} - \left(A_{port} \right)_{initial} \right] = \bar{\rho}_{fuel} \cdot L_{port} \left[\left(D_{0_{port}} + 2 \cdot s \right)^2 - D^2_{0_{port}} \right] \cdot \frac{\pi}{4} \quad . \tag{7}$$

Solving Eq. 7 for the total fuel regression gives

$$s = \frac{D_{0_{port}}}{2} \left(\sqrt{1 + \frac{\Delta M_{fuel}}{\bar{\rho}_{fuel} \cdot \left(A_{port} \right)_{initial} \cdot L_{port}}} - 1 \right) \quad . \tag{8}$$

In Eqs. (7) and (8) ρ_{fuel} is the mean fuel grain density, L_{port} is the length of the fuel port, A_{port} is the port cross sectional area, D_{0port} is the initial port hydraulic diameter, and s is the total linear regression of the fuel port. The mean density of the combined ignitor cap, Cu-infused fuel grain is calculated by

$$\bar{\rho}_{fuel} = \frac{\rho_{cap} \cdot \rho_{Cu-fuel}}{\rho_{Cu-fuel} \cdot \frac{M_{cap}}{M_{cap} + M_{Cu-fuel}} + \rho_{cap} \cdot \left(1 - \frac{M_{cap}}{M_{cap} + M_{Cu-fuel}} \right)} \quad . \tag{9}$$

In Eq. (8) the parameters M_{cap} and ρ_{cap} represent the initial mass and density of the of the 3-D printed fuel cap, and $M_{Cu\text{-}fuel}$ and $\rho_{Cu\text{-}fuel}$ are the initial mass and density of the of the Cu-infused fuel grain.

Table 2 lists the values for each of these parameters for the fuel cap and the Cu-infused fuel grains for various levels of copper content. The listed grain weights are averaged values. Depending on the quality of the print, the true initial weights varied slightly from grain-to-grain. The ABS injector cap, 3-D printed using the Fortus 250MC printer in the USU engineering design lab,[34] had a slightly lower print density than the baseline ABS fuel grains as printed by the previously-described Creality Ender 3 printer.

Table 2. Mass and Densities of the Various 3-D Printed Fuel Grain Components.

Fuel Grain	0% Cu	2% Cu	4% Cu	6% Cu
M_{cap}	11 g	11 g	11 g	11 g
ρ_{cap}	1.005 g/cm^3	1.005 g/cm^3	1.005 g/cm^3	1.005 g/cm^3
$M_{Cu-fuel}$	35.0 g	35.6 g	36.3 g	37.0 g
$\rho_{Cu\text{-}fuel}$	1.039 g/cm^3	1.058 g/cm^3	1.077 g/cm^3	1.097 g/cm^3
$M_{cap}+M_{Cu-fuel}$	46.0 g	47.6 g	47.3 g	48.0 g
$\overline{\rho}_{fuel}$	1.031 g/cm^3	1.045 g/cm^3	1.059 g/cm^3	1.074 g/cm^3

Given the total fuel regression over the burn, then longitudinal mean rate of fuel regression over the burn is estimated by

$$\overline{\dot{r}}_L = \frac{s}{t_{burn} - \tau_{latency}} . \tag{10}$$

In Eq. (10) t_{burn} is the total burn time, and $\tau_{latency}$ is the ignition latency after the oxidizer flow has initiated, typically 0.25 seconds for the fuel grains tested. Based on the total fuel regression, the effective post-burn diameter is estimated by

$$\overline{D}_{final} = \sqrt{D^2{}_{0_{port}} + \frac{4}{\pi}\frac{\Delta M_{fuel}}{\rho_{fuel}\cdot L_{port}}} . \tag{11}$$

The mean oxidizer massflux is estimated as

$$\overline{G}_{ox} = \frac{1}{t_{burn}}\left(\frac{\Delta M_{ox}}{\frac{\pi}{4}\cdot\overline{D}^2_{final}}\right), \tag{12}$$

and the total massflux exiting the fuel port is estimated by

$$\overline{G}_{total} = \frac{1}{t_{burn}}\left(\frac{\Delta M_{ox}}{\frac{\pi}{4}\cdot\overline{D}^2_{final}}\right) + \left(\frac{1}{t_{burn}-\tau_{latency}}\right)\cdot\left(\frac{\Delta M_{fuel}}{\frac{\pi}{4}\cdot\overline{D}^2_{final}}\right) . \tag{13}$$

The mean oxidizer level across the burn duration is estimated by

$$\left(O/F\right) = \frac{\Delta M_{ox}}{\Delta M_{fuel}} . \tag{14}$$

The mean delivered specific impulse over the burn duration is estimated by

$$I_{sp} = \frac{1}{g_0}\frac{\int_0^{t_{burn}} F\left(t\right)\cdot dt}{\Delta M_{ox}+\Delta M_{fuel}} . \tag{15}$$

The mean characteristic velocity over the burn duration is estimated by

$$c^* = \frac{\left[\int_0^{t_{burn}} P_0\left(t\right) - p_\infty \cdot dt + t_{burn}\cdot p_\infty\right]\cdot A^*}{\left(\Delta M_{ox}+\Delta M_{fuel}\right)} , \tag{16}$$

and the mean thrust coefficient over the burn duration is estimated by

$$C_F = \frac{\int_0^{t_{burn}} F\left(t\right)\cdot dt}{\left[\int_0^{t_{burn}} P_0\left(t\right) - p_\infty \cdot dt + t_{burn}\cdot p_\infty\right]\cdot A^*} . \tag{17}$$

In Eqs. (15) and (16), g_0 is the standard acceleration of gravity at sea level ($9.8067\ m/sec^2$), p_∞ is the local ambient pressure, and A^* is the choked nozzle throat area. These calculations assume no nozzle throat erosion during the burn.

PRELIMINARY TEST RESULTS

For all tests reported in this paper gaseous oxygen (GOX) was used as the oxidizer. To this point a total of 19 fuel grains with varying geometries and all 4 Cu-infusion densities (0%, 2%, 4%, 6%) have been tested. As a general conclusion metallization of the printed fuel

grains moderately increases the fuel regression rate, with negligible impact on the propellant characteristic velocity and the overall system specific impulse.

Example Burn Time Histories

As an example, Figure 7 compares two representative burn time histories for the test article using the fuel grains with the 6-lobed port. Figures 7(a)-a(d) present the burn time history of a baseline non-metallized fuel grain, and Figures 7(e)-7(h) shows the corresponding data for a fuel grain with a 6% Cu-infusion. Plotted are (a), (e) Thrust, (b), (f) Chamber Pressure, (c), (g) Total Impulse, and (h), Consumed Propellant mass. Note that both burns deliver thrust levels reach the designed 12-N level, but the burn using the metallized grain delivers a slightly high total impulse and associated chamber pressure.

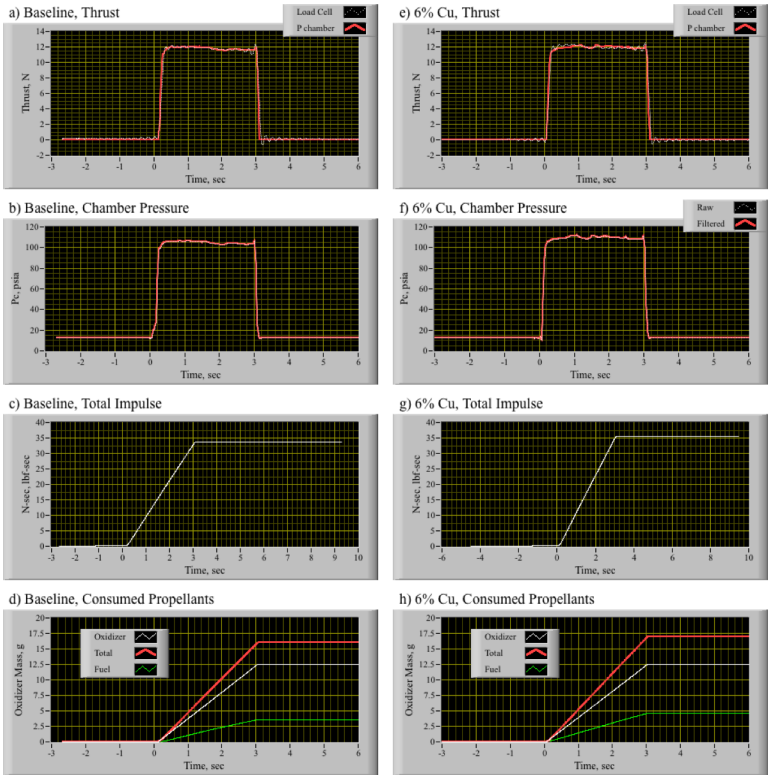

Figure 7. Comparing Burn Time Histories of 38-MM Thruster Burning ABS and GOX, Baseline versus 6% Cu-Infused Fuel Grains.

Close examination of Figures 7(d) and 7(h) identify the source of this increase. As shown by the white time history trace, burns exhibit identical oxidizer mass consumption - approximately 16 grams over the 3 second burn - but as shown by the green and red time history traces, burn consumes more of the Cu-infused fuel grain. This consumed-mass increase results partially from the increased fuel density, but is mostly due to an increased rate of fuel regression. The increased rate of fuel consumption causes the increase in both chamber pressure and the total delivered impulse for the Cu-infused fuel grain.

Table 3. Performance Comparisons for 38-mm Thruster with 0% and 6% Copper-Infused ABS Fuel Grains, as Derived from Data of Figure 7.

Fuel Grain	*I total* *N-s*	ΔM_{total} *grams*	P_0 *Avg psia*	C_F	c^* *m/sec*	I_{sp} *sec*	*O/F*
0% Cu	33.57	16.05	100.68	1.384	1510.5	213.2	3.49
6% Cu	35.59	17.03	107.24	1.385	1508.5	213.1	2.78

Effect of metallization on Thruster Performance

It must be noted that Cu-infusion of the ABS fuel grains will generally have the effect of measurably increasing the molecular weights and dropping the flame temperature of the combustion products. These changes should result in a measurable drop in the specific impulse and characteristic velocity. Counter intuitively, this lowered-performance result was not observed in this testing campaign. Table 3 shows this result. Note that the key performance metrics C_F, c^*, and I_{sp} for both of the burns of Fig. 7 are nearly identical, but the total delivered impulse (and mean thrust level) increases by more than 6% for the Cu-infused grain. Similar results are observed for all of the test comparisons.

Equilibrium Chemistry Analysis

The observed puzzling performance effects (due to metallization) can be better understood using equilibrium chemistry analysis. These calculations were performed using the industry-standard NASA thermo-chemical equilibrium code, CEA (Ref.[33]). Figures 8 and 9 plot the results for the baseline GOX/ABS propellants, and for GOX burned with 6% Cu-Infused ABS. The enthalpy of formation (*60.11 MJ/kg-mol*) and molecular weight (*62.95 kg/kg-mo)* of the ABS material were estimated using the methodology presented by Whitmore (2020).[35] and input into the CEA program for three different pressure level, 75 psia, 100 psia, and 125 psia; and O/F ratios varying from 0.5 to 5.

For the baseline fuel material Figure 8 plots pressure/OF profiles for the theoretical adiabatic flame temperature T_0, molecular weight M_W, and characteristic velocity c^*. Figure 9 presents the same calculations for the 6% Cu-infused fuel material. The stoichiometric O/F ratio and the mean operating O/F ratios for the cylindrical port and the 6-lobed star port fuel are also noted by the dashed-line and the red and blue symbols on each plot. Note that the metallized fuel grain exhibits a lowered overall set of c^* curves; however, due to the higher rate of fuel regression and a fuel-rich O/F ratio, the actual operating c^* *values are actually higher when compared to the baseline ABS.*

The current motor geometry is such that the motor burns with O/F ratios slightly higher than the stoichiometric point with the baseline propellants. When Cu is infused into the ABS fuel, the increased regression rate subsequently lowers the O/F ratio such that the motor burns richer, and the associated O/F drop lowers to lower the molecular weight substantially, with only a marginal drop in the adiabatic flame temperature. The resulting operating O/F value for the Cu-infused brains are actually closer to the optimal O/F ratio.

Thus, at least for this small snapshot of data it can be reasoned that the Cu-infusion measurable increases the mean thrust level and volumetric efficiency, with little detrimental effect on the mechanical and chemical efficiency of the system. It may be conjectured that neutral performance results shown by the unique characteristic of the small-scale legacy 38-mm thruster system, and this result may not hold for larger propulsion systems. More testing is clearly required in order to verify that the demonstrated increased-regression rate with performance effects due to Cu-infusion holds universally.

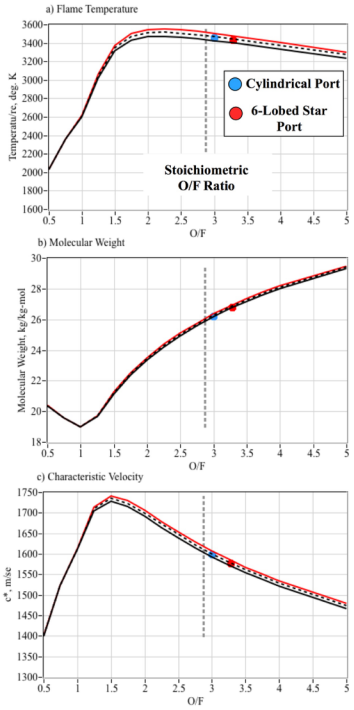

Figure 8. Equilibrium Chemistry Calculations for GOX/ABS Baseline Propellants.

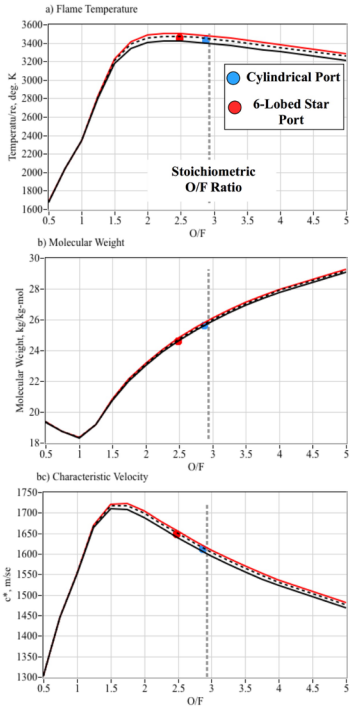

Figure 9. Equilibrium Chemistry Calculations for GOX/6%-Cu Infused ABS Baseline Propellants.

Fuel Regression Rate Summary

As presented in the previous section, because the legacy thruster system operates at relatively low O/F ratios for both the 6-lobed star and cylindrical fuel ports, the fuel massflow tends to make up a significant portion of the total chamber-exit massflow, and has a significant effect on the total fuel regression rate. This the fuel regression rate will be correlated with the total chamber exit massflux in this analysis.

Figure 10 summarizes the effects of Cu-metallization on the mean fuel regression rates, plotted as a function of the total massflux exiting the fuel port. The mass-based fuel regression rates are calculated by the methods of the previous section, Eqs. (8), (10), and total massflux is

calculated by Eq. (13). Figure 10(a) plots the data for the cylindrical port fuel grains, and Figure 10(b) presents similar comparisons for the 6-lobed star fuel grains. For both plots the dashed lines as plotted on these graphs result from power law mass-flux curve-fits of the form

$$\bar{\dot{r}}_L = a \cdot \bar{G}_{tot}^{\ n} \quad . \tag{18}$$

Table 4 summarizes the associated curve fit coefficients, where the power-law fit parameters *{a, n}* are listed as a function of the Cu-mass percentages for both of the port geometries. Of note from Table 4 is that the curve-fit burn exponents all have magnitudes that are near the critical value of $n = 1/2$, with the 6-Lobed start port grains having burn exponents slightly greater than *1/2*, and the cylindrical port grains having values less than *1/2*.

As noted by Zilliac and Karabeyoglu,[36] a hybrid motor with a burn exponent with magnitude less than *1/2* tends to burn richer with time. A hybrid motor with a burn exponent with magnitude greater than 1/2tends to burn leaner with time. Finally, a hybrid motor with a burn exponent of 1/2corresponds to a propellant combination with essentially no *O/F* shift over the burn lifetime. duration.

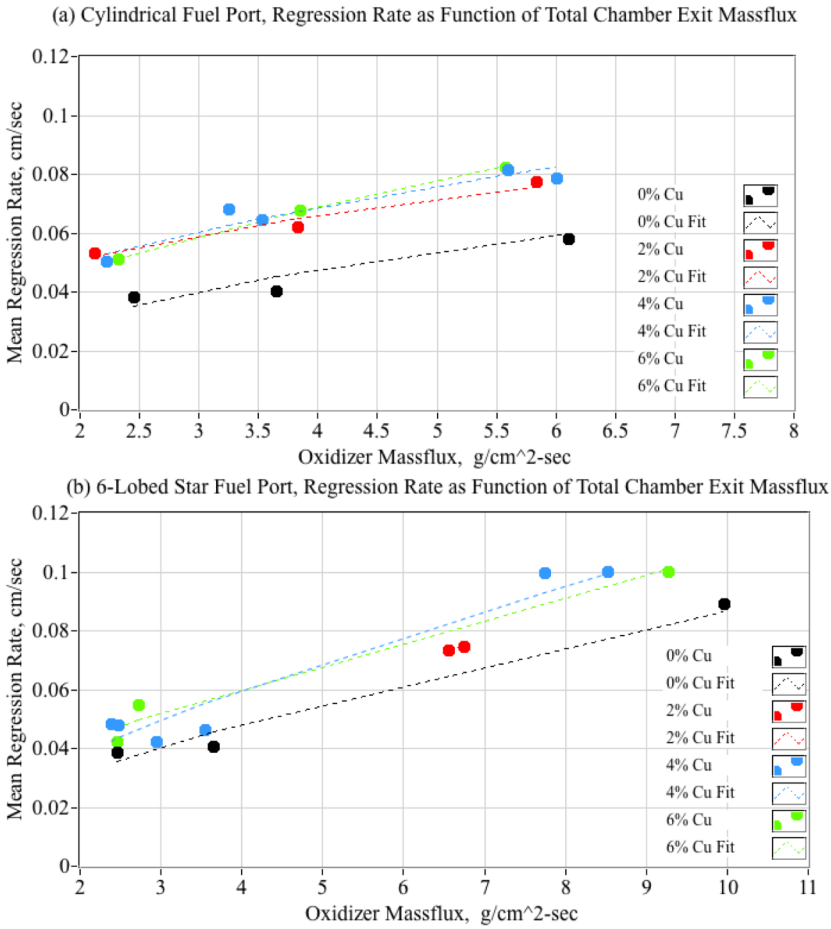

Figure 10. Regression Rates of Cylindrical and 6-Lobed Star Straight Port Geometry for Increasing Percentages of Cu-Metallization.

These numerical calculations agree well with the test observations from this burn series, where only small *O/F* shifts were noted over the burn lifetimes, with the cylindrical ports tending to burn richer with time, and the 6-Lobed Star ports tending to burn leaner with time.

Table 4. Regression Rate Power Law Parameter Summary

Port Geom.	*Para-meter*	*0% Cu*	*2% Cu*	*4% Cu*	*6% Cu*
Cylindrical Port	***a, cm/sec***	0.0240	0.0397	0.03719	0.0323
	n	0.4678	0.3658	0.4444	0.5483
6-Lobed Star Port	***a, cm/sec***	0.0202	0.0227	0.0238	0.0278
	n	0.6316	0.6265	0.6661	0.5792

Effect of Thermal Conductivity on the Fuel Regression Rate

There exists anecdotal evidence that the increase in the mean regression rate directly results from the increased thermal conductivity of the Cu-infused fuel materials. In order to illustrate this hypothesis, the total-massflux curve fits of Table 4 are used to re-calculate and plot the fuel regression rate as function of the Cu-mass percentages. Figure 11 shows this result for both of the fuel-port geometries.

For the cylindrical-port configuration data, Fig. 11(a) plots predicted fuel regression rate as function of Cu-mass parentages for three different massflux levels, *1, 5, and 9 g/cm^2-sec.* Also plotted by Fig 11(b) are the normalized fuel regression rates, calculated as the ratio

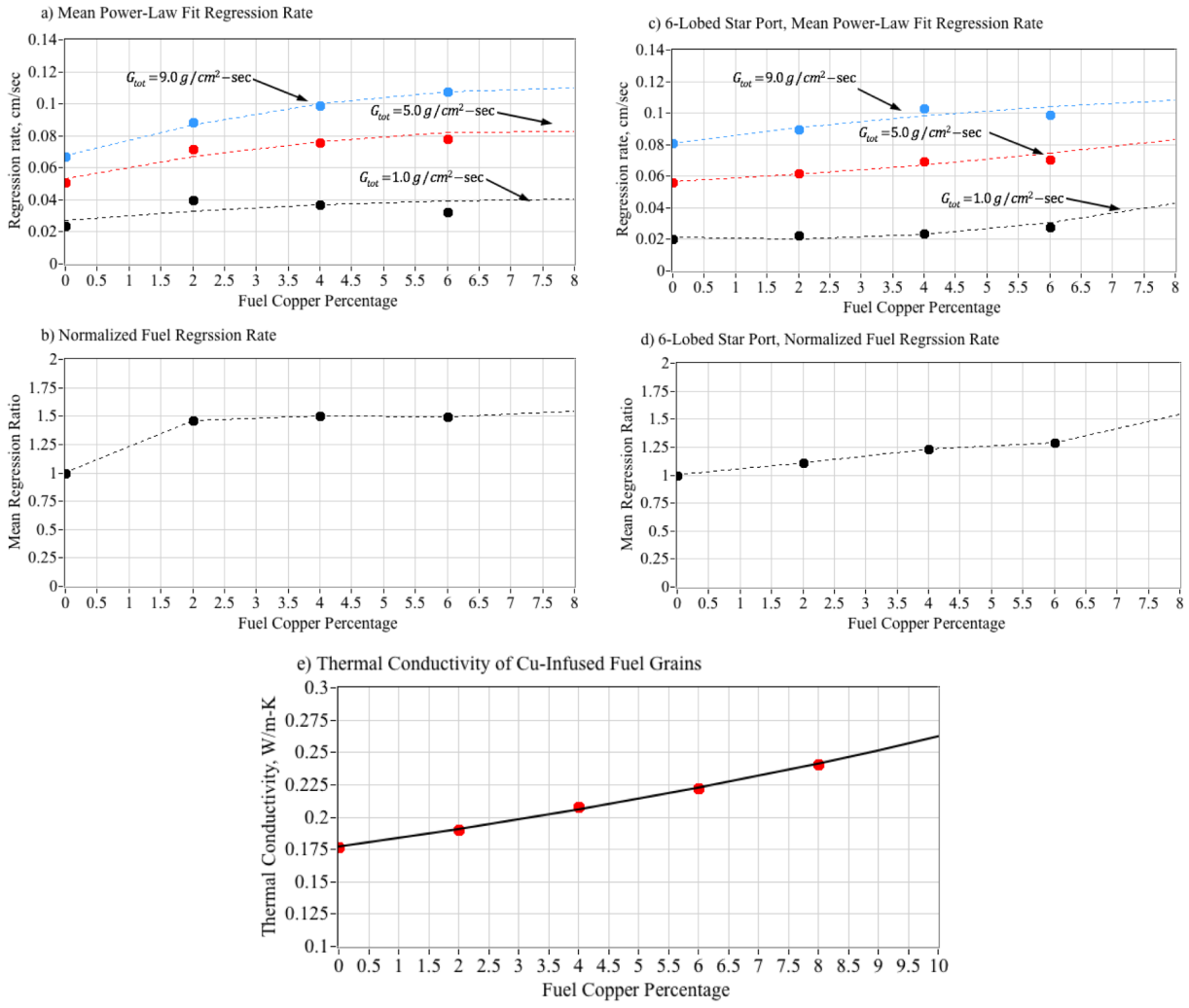

Figure 10. Exponential-Fit Regression Rates and Fuel-Class Thermal Conductivity as Function of Cu-Mass Percentages.

of the fuel regression rates at each Cu-mass percentage divided the regression rate of the non-metalized baseline ABS fuel over the three massflux levels. Figs. 11(c) and 11(d) plot the corresponding data for the 6-lobed star port configuration. Finally, Fig. 11(e) plots both the calculated and measured thermal conductivity of each fuel grain class as a function of the Cu-mass percentage. For this test series, the "3-omega[37]" method was used to measure the thermal conductivity of sample fuel grains, curt into thin strips.

The thermal conductivities of the Cu-infused ABS is calculated using Lichtenecker's mixing rule,[38,39] where

$$\log\left(\kappa_{Cu/ABS}\right)=\left(1-\varphi\right)\cdot\log\left(\kappa_{ABS}\right)+\varphi\cdot\log\left(\kappa_{Cu}\right)=\log\left(\kappa_{ABS}\right)+\varphi\cdot\left[\log\left(\kappa_{Cu}\right)-\log\left(\kappa_{ABS}\right)\right]. \tag{19}$$

In Eq. (19) $\kappa_{Cu/ABS}$ is the thermal conductivity of the Cu-infused fuel material, κ_{ABS} is the thermal conductivity of the baseline ABS material, approximately *0.177 W/m-K*; and κ_{Cu} is the thermal conductivity of elemental copper, approximately 397.5. *W/m-K*. The volume fraction occupied by the copper-filler can be calculated from the mass fraction and the material densities by

$$\varphi = \frac{\chi_M \cdot \left(\rho_{ABS}\right)}{\chi_M \cdot \left(\rho_{ABS}\right) + \left(1-\chi_M\right) \cdot \left(\rho_{Cu}\right)} \quad (20)$$

In Eq. (20) where, χM is the copper-mass concentration in the base ABS material, and ρ_{ABS}, ρ_{Cu} are the mean densities of the base materials, *1.039 g/cm*^{3}, and *8.94 g/cm*^{3}, respectively

Lichtenecker's mixing rule does account for the non-homogeneous topological peculiarities of the 3-D printed ABS dilled with the and filled with dispersed filler. Mamunya and Valeriy[40] suggest a simple scaling correction to account for this non-homogeneity, where

$$\log\left(\kappa_{Cu/ABS}\right) = \log\left(\kappa_{ABS}\right) + K \cdot \varphi \cdot \left[\log\left(\kappa_{Cu}\right) - \log\left(\kappa_{ABS}\right)\right]. \quad (21)$$

Solving for the thermal conductivity of the blended material gives

$$\kappa_{Cu/ABS} = \kappa_{ABS} \cdot \left(\frac{\kappa_{Cu}}{\kappa_{ABS}}\right)^{K\varphi} \quad (22)$$

A scale factor of K=4 gives a best fit to the measured thermal conductivities.

Note that on Figure 11, that for both port configurations there exists a clear trend of increasing regression rate as a function of Cu-mass percentage. There also exists a high level of correlation between the increasing fuel regression rates, and the increase in thermal conductivity due to Cu-infusion into base ABS fuel material. Finally, there also appears to be a limiting-point whereby infusing additional Cu into the base material provides diminishing benefits.

PROPOSED FUTURE WORK AND FOLLLOW-ON ACTIVITES

When quantified though additional testing, the increased burn rate and overall increase in solid-fuel density resulting from metallization will allow a measurable increase in the propellant density impulse. Due to the demonstrated success of the research campaign at this point, no major changes in the test plan or test matrix are proposed. The go forward plan is to continue testing, collecting sufficient numbers of test results to allow formal statistical assessments to be established. Marxman-style[41] regression rate models will be modified to introduce conductive heat transfer - due to the increased thermal conductivity of the metalized fuels - into the enthalpy balance models. Predicted fuel regression rates from the modified models will be correlated to measurements.

Following the successful completion of the above-listed project objectives, it is proposed to investigate the practicality and potential benefits of infusing advanced materials like carbon- nanotubes, graphene,[42] and MXenes (i.e., 2D transition metal carbides/carbonitrides/nitrides)[43] into the polymer matrix. The anisotropic properties of these materials can potentially be leveraged to design hybrid fuel structures with exceptionally high regression rates, and strategic alignment of the additives may allow more uniform burn rates along the fuel port length. When pyrolyzed, the carbon-based additives will also provide a low molecular weight fuel source in addition to the thermoplastic; potentially also increasing in the fuel characteristic velocity and specific impulse.

SUMMARY AND CONCLUSION

It is well documented in technical literature that hybrid rocket systems generally have fuel regression rates that are typically 25-30% lower than solid fuel motors in the same thrust and impulse class. Lowered fuel regression rates tend to produce unacceptably low equivalence ratios that lead to poor mass-impulse performance, erosive fuel burning, nozzle erosion, reduced motor duty cycles, and potential combustion instability. To achieve equivalence ratios resulting in acceptable combustion characteristics, hybrid fuel ports are often fabricated with very long length-to-diameter ratios. The resulting poor volumetric efficiency is incompatible with Small Satellite (SmallSat) applications.

This paper present preliminary results a development campaign, whereby modern extrusion and 3-D printing techniques are used to fabricate sample ABS fuel grains with varying levels of copper-metallization. Fuel grains with two different fuel port geometries (1) a cylindrical fuel port and (2) a 6-lobed star fuel port cross-section, were manufactured and tested. The fabricated fuels are currently being tested by USU's Propulsion Research laboratory using a legacy 38-mm, 12-N hybrid thruster system previously designed for small spacecraft applications.

Fabrication and manufacturing methods are described, and results of hot fire tests are presented. The top-level conclusion is that metallization of the printed fuel grains moderately increases the fuel regression rate, with negligible impact on the propellant characteristic velocity and the overall system specific impulse. The increased burn rate and overall increase in solid-fuel density resulting from metallization will allow a

measurable increase in the propellant impulse-density. This result is potentially significant for small spacecraft and other applications where volumetric efficiency has a premium value.

The presented test results exhibit compelling evidence that metallization of the printed fuel grains measurably increases the fuel regression rate, with negligible impact on the propellant characteristic velocity and the overall system specific impulse. Before the testing campaign, it was expected that Cu-infusion of the ABS fuel grains would have the effect of measurably lowering the combustion flame temperature and increasing the molecular weights and dropping the flame temperature of the combustion products. These changes should result in a measurable drop in the specific impulse and characteristic velocity. Counter intuitively, this lowered-performance result was not observed in this testing campaign.

The current motor geometry is such that the motor burns with O/F ratios slightly higher than the stoichiometric point with the baseline propellants. When Cu is infused into the ABS fuel, the increased regression rate subsequently lowers the O/F ratio such that the motor burns richer, and the associated O/F drop lowers to lower the molecular weight substantially, with only a marginal drop in the adiabatic flame temperature. The resulting operating O/F value for the Cu-infused grains are actually closer to the optimal O/F ratio.

There exists anecdotal evidence that the increase in the mean regression rate directly results from the increased thermal conductivity of the Cu-infused fuel materials. The test results exhibit a high level of correlation between the increasing fuel regression rates, and the increase in thermal conductivity due to Cu-infusion into base ABS fuel material. These does, however, also appear to be a limiting-point whereby infusing additional Cu into the base material provides diminishing benefits.

Thus, at least for the presented ensemble of data, it can be reasoned that the Cu-infusion measurably increases the mean thrust level and volumetric efficiency, with little detrimental effect on the mechanical and chemical efficiency of the system. It may be conjectured that neutral performance results shown by the unique characteristic of the small-scale legacy small-thruster system used for this campaign, and this result may not hold for larger propulsion systems. More testing is clearly required in order to verify that the demonstrated increased-regression rate with performance effects due to Cu-infusion holds universally.

1. Whitmore, Stephen A., "Additive Manufacturing as an Enabling Technology for "Green" Hybrid Spacecraft Propulsion," RAST-1039*, Conference on Recent Advances in Space Technology 2015*, Istanbul Turkey, June 16-19 2015. https://ieeexplore.ieee.org/document/7208305
2. Whitmore, Stephen A., Merkley, Stephen L., Zachary S., Walker, Sean D., "Development of a Power Efficient, Restartable, "Green" Propellant Thruster for Small Spacecraft and Satellites," SSC15-P-34, *29th AIAA/USU Conference on Small Satellites*, Logan UT, 8-13 August, 2015. https://digitalcommons.usu.edu/smallsat/2015/all2015/90/
3. Whitmore, S. A., "Three-Dimensional Printing of "Green" Fuels for Low-Cost Small Spacecraft Propulsion Systems," *J. Spacecraft and Rockets*, Vol. 54, No. 6, 2017, https://doi.org/10.2514/1.A33782
4. Cheng, C. G., Farmer, R. C., Jones, H. S., and McFarlane, J. S., "Numerical Simulation of the Internal Ballistics of a Hybrid Rocket," AIAA Paper 94-0554, *30th AIAA/ASME /SAE/ASEE Joint Propulsion Conference & Exhibit*, Indianapolis, IN, July, 1994. https://doi.org/10.2514/6.1994-554
5. Karabeyoglu, M. A., "Hybrid Rocket Propulsion for Future Space launch," *Stanford University Aero/Astro 50th Year Anniversary Presentation*, May 09, 2008, http://aa.stanford.edu/events/50thAnniversary/media/Karabeyoglu.pdf, [Retrieved 23 December 2013].
6. Fiedler, R. A., Breitenfeld, M. S., Jiao, X., Haselbacher, A., Geubelle, P., Guoy, D., and Brandyberry, M., "Simulations of Slumping Propellant and Flexing Inhibitors in Solid Rocket Motors," AIAA-2002-4341, *38th AIAA/ASME/SAE/ASEE Joint Propulsion Conference & Exhibit*, 07 July 2002 - 10 July 2002, Indianapolis, Indiana. *https://doi.org/10.2514/6.2002-4341.*
7. Karabeyoglu M. A., Stevens, J., and Cantwell B. J., "Investigation of Feed System Coupled Low Frequency Combustion Instabilities in Hybrid Rockets," AIAA 2007-5366, *43rd AIAA/ASME/SAE/ASEE Joint Propulsion Conference & Exhibit, 8 - 11 July 2007, Cincinnati, OH. https://doi.org/10.2514/6.2007-5366*
8. Whitmore, Stephen A., Walker Sean D., Merkley Daniel P., and Sobbi, Mansour, "High Regression Rate Hybrid Rocket Fuel Grains with Helical Port Structures,"AIAA-2014-3751, *50th AIAA/ASME/SAE/ASEE Joint Propulsion Conference and Exhibit*, Cleveland OH, 28-30 July 2014. https://doi.org/10.2514/1.B35615
9. Whitmore, Stephen A., and Walker Sean D., "High Regression Rate Hybrid Rocket Fuel Grains with Helical Port Structures," J. *Prop. & Power*, Vol. 31, No. 6, 2015, pp. 1727-1738, https://arc.aiaa.org/doi/abs/10.2514/1.B35615.
10. Lee, T. S., and Potapkin, A., "The performance of a Hybrid Rocket with Swirling GOX Injection," Aerospace Science and Technology Research Center Report Number ADA 409123, August 2002, *http://www.dtic.mil/cgi-bin/GetTRDoc?AD=ADA409123, [Retrieved 14 February 2014].*
11. Knuth, W. H., Chiaverini, M. J., Sauer, J. A., and Gramer, D. J., "Solid-Fuel Regression Rate Behavior of Vortex Hybrid Rocket Engines", *Journal of Propulsion and Power*, Vol. 18, No. 3, 2002, pp. 600-609. https://doi.org/10.2514/2.5974
12. Karabeyoglu M. A., Altman D., Cantwell B. J., "Combustion of Liquefying Hybrid Propellants: Part 1, General Theory," *Journal of Propulsion and Power*, Vol. 18, No. 3, March, 2002, pp. 610-620. https://doi.org/10.2514/2.5975
13. [13] Nakagawa, I., Hikone, S., and Suzuki, T., "A Study on the Regression Rate of Paraffin-based Hybrid Rocket Fuels," AIAA 2009-4935, *45th AIAA/ASME /SAE/ASEE Joint Propulsion Conference & Exhibit*, Denver, CO, 28 July-1 August 2009. https://doi.org/10.2514/1.B34206

14. Karabeyoglu, M. A., Zilliac, G., Cantwell, B. J., Dezilwa, S., and Castellucci. P., "Scale-up Tests of High Regression Rate Paraffin-Based Hybrid Rocket Fuels," *Journal of Propulsion and Power*, Vol., No. 5, pp. 1037-1045, Nov.-Dec., 2004. https://doi.org/10.2514/1.3340

15. Kosanke, K., von Maltitz, I., Kosanke, B. J., Shimizu, H. T., Dillehay, D. R., T. S. Jennings-White, and Chapman, D., "Pyrotechnic Chemistry," *J. Pyrotechnic Chemistry*, 2004, ISBN 1889526150, ISBN 97818892526157.

16. Karabeyoglu, M. A., and Arkun, Ugur, "Evaluation of Fuel Additives for Hybrid Rockets and SFRJ System," AIAA 2014-3647, *AIAA Propulsion and Energy Forum,* July 28-30, 2014, Cleveland, OH 50th AIAA/ASME/SAE/ASEE Joint Propulsion Conference. https://doi.org/10.2514/6.2014-3647.

17. Material Data Center, Cycolac Resin MG94,™ Safety Data Sheet, https://www.materialdatacenter.com/ms/en/tradenames/Cycolac/. [Retrieved 28 January, 2021].

18. Filastruder, MG94 ABS Natural Pellets, https://www.filastruder.com/collections/pellets/products/mg94-abs-natural-pellets. [Retrieved 28 January, 2021].

19. EnvironMolds, LLC, Linkedin, https://www.linkedin.com/company/environmolds-llc. [Retrieved 28 January, 2021].

20. Creality, 3-D Ender Printer, https://creality3d.shop/. [Retrieved 28 January, 2021].

21. Whitmore, S.A., Stoddard, R.L., "N2O/O2 blends safe and volumetrically efficient oxidizers for small spacecraft hybrid propulsion," *Aeronaut. Aerosp. Open Access J.* 2019, Vol.2, No. 3. https://medcraveonline.com/AAOAJ/AAOAJ-03-00097.pdf. [Retrieved 5 May 2020].

22. Stoddard, R. L., "Experimental Investigation of N2O/O2 Mixtures as Volumetrically Efficient Oxidizers for Small Spacecraft Hybrid Propulsion Systems," Master's Thesis, *Utah State University Digital Commons*, December 2019. https://digitalcommons.usu.edu/. [Retrieved May 2020].

23. Whitmore, Stephen A., "Nytrox as "Drop-in" Replacement for Gaseous Oxygen in SmallSat Hybrid Propulsion Systems," Aerospace 2020, Vol. 7, No. 43. https://dor.org/10.3390/aerospace7040043.

24. Palermo, E., "Fused Deposition Modeling: Most Common 3D Printing Method," LIVESCIENCE, September 19, 2013, https://www.livescience.com/39810-fused-deposition-modeling.html, [Retrieved 02 December, 2019].

25. Whitmore, *S. A.,* Inkley, *N. R.,* Merkley, *D. P.,* and Judson*, M. I.,* "Development of a Power-Efficient, Restart-Capable Arc Ignitor for Hybrid Rockets", *J. of Propulsion and Power*, Vol. 31, No. 6 (2015), pp. 1739-1749. https://dio.org/10.2514/1.B35595

26. Whitmore, S. A., Mathias, S. D., and Harvey, R., "High Voltage Breakdown and Arc-Tracking Mechanism of Thermoplastics with Applications to Hybrid Rocket Arc- Ignition," *53rd AIAA/SAE/ASEE Joint Propulsion Conference*, 10-12 July 2017, Atlanta, GA. AIAA 2017-4601. https://doi.org/10.2514/6.2017-4601

27. Whitmore, S. A., "Three-Dimensional Printing of "Green" Fuels for Low-Cost Small Spacecraft Propulsion Systems," *J. of Spacecraft and Rockets*, Vol. 54, No. 6 (2017), https://doi.org/10.2514/1.A33782.

28. Whitmore, Stephen A., "Additive Manufacturing as an Enabling Technology for "Green" Hybrid Spacecraft Propulsion," RAST-1039*, Conference on Recent Advances in Space Technology 2015*, Istanbul Turkey, June 16-19 2015. https://ieeexplore.ieee.org/document/7208305

29. Whitmore, Stephen A., Merkley, Stephen L., Zachary S., Walker, Sean D., "Development of a Power Efficient, Restartable, "Green" Propellant Thruster for Small Spacecraft and Satellites," SSC15-P-34, *29th AIAA/USU Conference on Small Satellites*, Logan UT, 8-13 August, 2015. https://digitalcommons.usu.edu/smallsat/2015/all2015/90/

30. Anon., "ULTRAVOLT C Series High Voltage CAP-Charging Supplies," Advanced Energy, Inc.,

https://www.advancedenergy.com/globalassets/resources-root/data-sheets/ultravolt-c-series-data-sheet.pdf[Retrieved 9 May 2020].

31. Mathias, S. D., Whitmore, S. A., and Harvey, R., "High Voltage Breakdown and Arc-Tracking Mechanism of Thermoplastics with Applications to Hybrid Rocket Arc- Ignition," *AIAA 2017-4601, 53rd AIAA/SAE/ASEE Joint Propulsion Conference*, 10-12 July 2017, Atlanta, GA. https://doi.org/10.2514/6.2017-4601
32. Anderson, J. D., *Modern Compressible Flow*, 3rd Edition, New York: The McGraw Hill Companies, Inc., 2003, Chapters 4, 5, pp. 127-187. ISBN-13: 978-0072424430. https://libcat.lib.usu.edu/search/i0070016542
33. Gordon, S., and McBride, B. J., "Computer Program for Calculation of Complex Chemical Equilibrium Compositions and Applications," *NASA Technical Report RP-1311*, 1994. https://ntrs.nasa.gov/archive/nasa/casi.ntrs.nasa.gov/19950013764.pdf.
34. Engineering Design Lab, https://engineering.usu.edu/students/engineering-design-lab/3d-printing. [Retrieved 29 January, 2020].
35. Whitmore, S. A., "A Variational Method for Estimating Time-Resolved Hybrid Fuel Regression Rates from Chamber Pressure," AIAA 2020-3762, *AIAA Propulsion and Energy 2020 Forum*, August 2020. https://arc.aiaa.org/doi/abs/10.2514/6.2020-3762.
36. Zilliac, G.; Karabeyoglu, M.A. "Hybrid Rocket Fuel Regression Rate Data and Modeling," AIAA 2006-4504. *42nd AIAA/ASME/SAE/ASEE Joint Propulsion Conference & Exhibit, Sacramento*, CA, USA, 9–12 July 2006. https://doi.org/10.2514/6.2006-4504.
37. Linseis, Methods, "3-Omega Measurement Techniques, https://www.linseis.com/en/methods/3-omega-method.[Retrieved 19 May 2021].
38. K. Lichtenecker, "Dielectric constant of natural and synthetic mixtures," *Phys Z*, vol. 27, pp. 115-158, 1926.
39. Goncharenko, A. V., Lozovski, V. Z., and Venger, E. F., " Lichtenecker's equation: applicability and limitations," Elsevier, Optics Communications, Vol. 174, 2000 pp. 19–32, www.elsevier.comrlocateroptcom, http://iht.univ.kiev.ua/library/papers-pdf/OpticsComm_174_19_2000.pdf. [Retrieved 2 February, 2021.
40. Mamunya, Y. P., and Valeriy, D., "Electrical and Thermal Conductivity of Polymers Filled with Metal Powders," *European Polymer Journal*, Vol. 38, No. 09, 2002, pp. 1887-1897. https://doi.org/10.1016/S0014-3057(02)00064-2.
41. Marxman, G. and Gilbert, M., "Turbulent Boundary Layer Combustion in the Hybrid Rockets" *Symposium (International) on Combustion*, Vol. 9, no. 1., 1963, pp. 371–383. https://doi.org/10.1016/S0082-0784(63)80046-6
42. Gnanasekarana, K., Heijmansab, T., van Bennekomb, S., Woldhuisb, H., Wijniab, S., de Witha, J., Friedricha, H., "3D printing of CNT- and graphene-based conductive polymer nanocomposites by fused deposition modeling," Materials Today, Vol. 8-9, December 2017, pp. 21-28. https://doi.org/10.1016/j.apmt.2017.04.003.
43. Naguib, M.; Mochalin, V.N.; Barsoum, M.W.; Gogotsi, Y., "25th Anniversary Article: MXenes: A New Family of Two- Dimensional Materials". *Advanced Materials*. Vol. 26, No. 7, 2011, pp. 992–1005. https://onlinelibrary.wiley.com/doi/abs/10.1002/adma.201304138.